

Co-precipitation synthesis and characterization of rare-earth pyrochlore Gadolinium stannate; A novel electrocatalyst for the determination of furazolidone in water samples

Karupiah Balamurugan¹, Ramachandran Rajakumaran¹, and Shen Ming Chen^{1,*},
Tse-Wei Chen^{1,2}, Po-Jui Huang¹

¹ Electroanalysis and Bioelectrochemistry Lab, Department of Chemical Engineering and Biotechnology, College of Engineering, National Taipei University of Technology, No. 1, Section 3, Chung-Hsiao East Road, Taipei 106, Taiwan, ROC.

² Research and Development Center for Smart Textile Technology, National Taipei University of Technology, Taipei 106, Taiwan, ROC.

*E-mail: smchen78@ms15.hinet.net (S-M Chen)

Received: 6 November 2020 / Accepted: 22 December 2020 / Published: 31 January 2021

Researchers are now increasingly concerned with the development of a resourceful and eminent catalyst for the trace level analysis and detoxification of toxic contaminants in the ecosystem. On keeping this in mind, we have efficiently prepared a novel pyrochlore phase gadolinium stannate ($Gd_2Sn_2O_7$; GDS) nanoparticles by a simple co-precipitation process and the electrochemical activity of prepared GDS nanoparticles against furazolidone (FUD) was proclaimed. The synthesized GDS nanoparticles were characterized by utilizing powder X-ray diffraction (PXRD), Raman spectroscopy, and X-ray photoelectron spectroscopy (XPS) analysis. The morphology of as-synthesized GDS nanoparticles was studied by field-emission scanning electron microscopy (FE-SEM) combined with energy-dispersive X-ray spectroscopy (EDX) and high-resolution transmission electron microscopy (HR-TEM). The GDS nanoparticles have been coated on the surface of a screen-printed carbon electrode and the GDS modified SPCE electrode (GDS/SPCE) has been hooked as a functional (working) electrode for the electrocatalytic sensor studies towards FUD. To analyze the electrocatalytic activity of GDS nanoparticles for the detection of FUD, electroanalytical techniques such as cyclic voltammetry (CV) and differential pulse voltammetry (DPV) have been practiced. The fabricated GDS/SPCE sensor established remarkable selectivity and sensitivity for the detection of FUD, which might be due to the great affinity of the cubic pyrochlore property of GDS nanoparticles. The fabricated sensor exposed two linear ranges from 0.01-153.21 μM and 193.21-1033.21 μM along with LOD (lower detection limit) of 23 nm and has an excellent sensitivity of 0.66 $\mu A \mu M^{-1} cm^{-2}$. The fashioned GDS modified SPCE sensor revealed outstanding repeatability, stability, and reproducibility for the detection of FUD. On affording the above-acquired findings, we hopefully tested our designed sensor for the real-time sensing analysis in water samples and obtained acceptable recovery results.

Keywords: Pyrochlore oxide, Gadolinium stannate nanoparticles, electrochemical sensor, FUD detection, real sample analysis, tap and, lake water.

1. INTRODUCTION

In modern medical research, antibiotics were considered as one of the most important discoveries in pharmaceutical applications [1]. Antibiotics act as an important drug for the prevention and treating bacterial infections, by either inhibiting or killing the growth of bacteria. During the past three decades, the need for veterinary antibiotics had been dramatically increased for treating disinfections and promoting the growth production among poultry farming [2, 3]. Furthermore, china used a huge amount of antibiotics (162,000) in 2013, making it the world's leading manufacturer and user of antibiotics [4, 5]. Due to mishandling and overdosage consumption of antibiotics among humans, it causes a serious threatening problem including allergies, nausea, arrhythmias, and loss of hearing [6, 7]. The antibiotics residues were entered directly into the natural ecosystem by excretion of animal wastes from husbandry, which potentially affects all living organisms and aquatic resources such as lake water, river water, and groundwater [8, 9, 10, 11]. Nitrofurans family is a type of antibiotic drug and widely used as an animal feed additive for treating the gastrointestinal infections produced by *E. coli* and *S. enterica* [12]. In many developed countries like Thailand (2002), European Union (1990), Australia (1993), Brazil (2002), and United States (2002), are strictly banned the practical use of nitrofurans due to its harmful side effects causing mutagenicity and carcinogenicity among food production animal industries [13]. The commonly used nitrofurans antibiotics drugs are nitrofurazone, nitrofurantoin, and furazolidone for their potential metabolic action against bacterial infections [14]. Consequently, the oral intake of such antibiotics is metabolized rapidly and it tends to remain in the human body system as tissue and protein-bound residue for a prolonged period, which may lead to serious health effects [15].

Among them, furazolidone (FUD) is a widely used chemotherapeutic medication for treating common infections in humans and animals over 30 years [16]. FUD (3-(5-nitrofurfurylideneamino)-2-oxazolidinone) having nitro group structure (Fig. 1), it has been commonly given as antiprotozoal and antibacterial nutrient supplement for animal husbandries and aquatic farming industries [17]. On crossing, the permissible dosage of FUD causes serious side effects in human beings by hindering the functions of the liver and kidney and it may lead to hepatotoxicity [18]. In the development of medical research, FUD shows reliable carcinogenic effects, and concerning human health risk, it is strictly prohibited in many countries [19]. The nitro free radicals ($\text{RNO}^{2\cdot-}$) produced from the metabolite residues of FUD can damage the DNA and it may induce cytotoxicity and carcinogenic effects [20, 19]. Therefore, the determination of the FUD is important among researchers to periodically monitor the residues of the hazardous antibiotics in an aquatic natural ecosystem, to maintain balanced environmental resources. Many analytical instruments and methods have been historically used for the estimation of FUD namely, LC-MS [21], HPLC [22], fluorimetry [23], spectrophotometry [24], and electrochemical sensing [25, 26].

In particular, electrochemical sensors offer vast advantageous factors such as portability, high selectivity, excellent sensitivity, reproducibility, rapid performance, trace level detection, and so on [27-34]. However, it is known that certain electroanalytical techniques had been studied for FUD sensing and determination. Hence, the researchers are investing so much effort to develop a novel and excellent

electrocatalytic material for the fabrication of sensors with wide electrochemical sensing properties. At present, rare-earth oxides have attained significant importance as an outstanding potential material in the research field of electrochemistry.

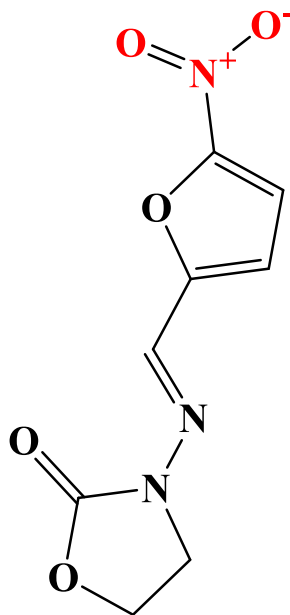


Figure 1. Chemical structure of furazolidone (FUD).

In general, Pyrochlore oxides belong to the group of isostructural compounds with a molecular formula known to be $A_2B_2O_7$, where “A” constitutes rare earth element adopts +3 oxidation state and “B” constitutes transition element adopts +4 oxidation state [35]. Here, the very different ionic radii drive the ordering of “A and B” cations on their corresponding lattice site [36]. The beneficial usage of pyrochlore compositions is considered a promising waste form and it is related to their outstanding structural flexibility as well as compositional diversity [37]. Among the various pyrochlore oxide chemistry, the lanthanide stannate pyrochlore ($Ln_2Sn_2O_7$; $Ln = Y, La-Lu$) occupies an important family with its unique cubic unit cell arrangement (Fd3m symmetry) [38, 39]. In recent years, the number of oxides of pyrochlore possesses interesting electrical, optical, catalytic, and magnetic properties [38]. They act as a potential functional material with dramatic applications in various research fields including magnetic frustration/spin ices, dielectrics, superconductivity, ionic conductors, phosphors, Li-ion batteries, optical emission, high-temperature pigments, and metal-semiconductor transitions [39, 40]. More fascinatingly, the lanthanide tin oxide pyrochlores retain high thermal stability and melting points, and therefore it is widely used for combustion gas control and automobile exhaust gas in an environment coupled with high-temperature catalytic applications ($> 2000\text{ }^\circ\text{C}$) [41]. For organic compounds degradation and the water-splitting process, the lanthanide pyrochlore showed enhanced photocatalytic activity [42]. The pyrochlore type oxide withholds significant technological importance in the hot fields of electrochemical devices namely solid oxide fuel cells. Tailoring the pyrochlore structure in their

respective lattice sites by metal ions substitutions induces a defective nature and it dramatically explores its utilization in ferroelectrics and gas sensors [43-46].

Until now, lanthanide pyrochlore stannates are commonly prepared by conventional solid-state reactions of tin oxide at elevated temperatures (about 1500 °C) for a prolonged time of 5 days [38]. Due to the requirement of high-energy consumption in the solid-state reactions, the resulting product will be agglomerated, which results in compositional inhomogeneity [47]. An optional synthetic pathway is a need for the effective preparation of pyrochlore stannate oxide. Currently, few more synthesis methods such as the sol-gel process [48], hydrothermal method [43, 49], and aerosol pyrolysis [50] have been employed.

In this present work, we have successfully prepared a pyrochlore phase-pure gadolinium stannate oxide nanoparticle, $Gd_2Sn_2O_7$ (GDS) with a facile and cost-effective co-precipitation synthesis pathway. The as-synthesized GDS were characterized and proved by numerous analytical approaches including such as PXRD, Raman, and XPS studies. The morphological investigations of GDS are observed by FE-SEM and HR-TEM microscopic studies. The as-prepared GDS delivers exceptional electrocatalytic behavior for the sensing of antibiotic drug FUD. The lake and river water were tested for realistic usability of the designed sensor for real-time sensing of FUD.

2. EXPERIMENTAL SECTION

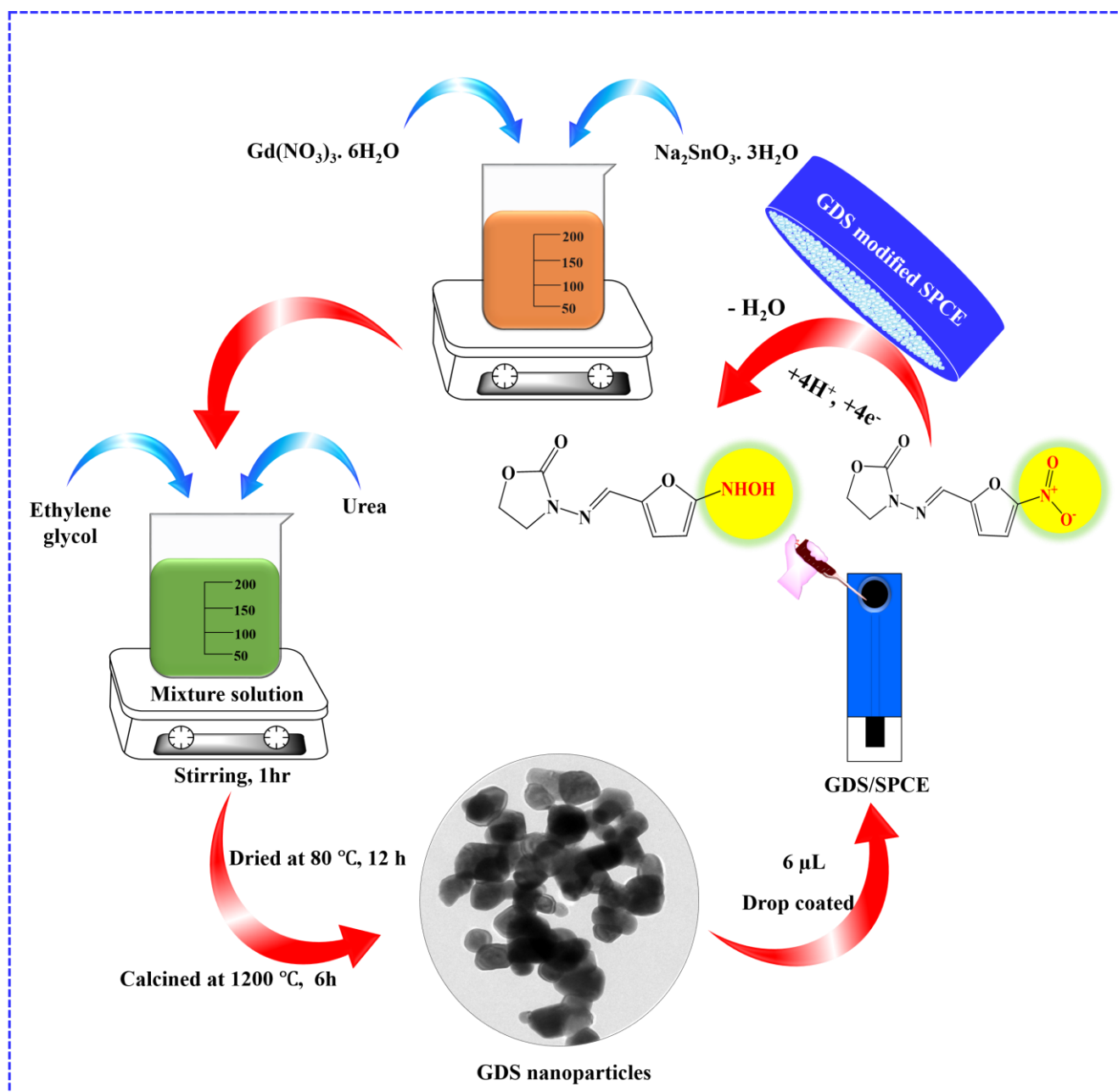
2.1. Materials

Sodium stannate trihydrate ($Na_2SnO_3 \cdot 3H_2O$), Gadolinium nitrate hexahydrate ($Gd(NO_3)_3 \cdot 6H_2O$), urea (CH_4N_2O), ethylene glycol ($C_2H_4O_2$), and all the remaining synthetic compounds have been collected from Sigma-Aldrich and utilized with no other sanctification process. In Zensor R&D Co., Ltd, Taiwan, SPCE (model SE 100, working surface area: 5 mm/0.196 cm²) was brought and used for the electrochemical analysis. The phosphate buffer solution (PBS) concentration of about 0.05 M as an auxiliary electrolyte for the complete studies using disodium hydrogen phosphate and sodium dihydrogen phosphate. Both solvents and chemical reagents were of high purity and used without additional detoxification. The necessary solutions for the experiments were prepared with the aid of double-distilled (DD) water for the entire experiment.

2.2. Co-precipitation synthesis of GDS nanoparticles

The GDS nanoparticles have been synthesized according to the following procedure. Initially, 0.1 M of $Gd(NO_3)_3$ was ionized in 50 ml of DD water. On the other hand, 50 ml of an aqueous solution of 0.2 M Na_2SnO_3 was added dropwise to the above solution. Followed by this process, urea of about 5g was weighed and dissolved in 10 ml aqueous solution and ethylene glycol (7 ml) were mixed and gently added into the metal precursor solution. The resultant mixture solution was allowed to stir continuously at 1000 rpm at room temperature for 1 hour. After that, the collected white-colored product was scrupulously washed by successive amounts of water and ethanol eventually, to wipe out the unreacted

molecules and impurities. Then, the resultant white hydrated sample was centrifuged and allowed to dehydration process in the hot air oven at 80 °C for 12 hours. Furthermore, the obtained product was crystallized in the muffle furnace by maintaining a constant temperature at 1200 °C for 6 hours. Finally, the resultant white-colored product was stored in an airtight glass vial and further used up for the experimental studies. The complete synthesis procedure for the preparation and its electrocatalytic applications of GDS nanoparticles was pictured in scheme 1.



Scheme 1. Detailed co-precipitation preparation method for GDS nanoparticles and their electrocatalytic applications.

2.3. Electrode fabrication process

For the fabrication process, 5 mg/ml of GDS nanoparticles have been dispersed and sonicated for 20 minutes, to acquire a homogenous solution. Before the surface modification process, the bare SPCE was well washed with a surplus amount of DD water. After that, a homogenous aliquot of GDS suspension of about 6 μL was drop coated on the pre-cleaned SPCE surface and the GDS fabricated SPCE was dried in a hot air oven, which is maintained at 50 $^{\circ}\text{C}$. Finally, the resultant GDS nanoparticles fabricated SPCE has been utilized as an operational electrode for further electrocatalytic investigations.

2.4. Analytical characterization

The crystallinity and purity of the as-synthesized GDS nanoparticles were analyzed by using PXRD with DMAX-III A diffractometer ($\lambda = 0.15406$ nm). The texture and the surface morphology of the GDS nanoparticles have been explored by FE-SEM studies using a ZEISS Sigma 300. The high-resolution transmission electron microscope, elemental mapping, and EDX analysis have been performed using HR-TEM: JEOL 2100F. The vibration and rotational modes of as-synthesized GDS nanoparticles were analyzed by Raman spectroscopy by using DONGWOO, Ramboss 500i micro-Raman/PL spectroscopy. Then XPS, (Thermo-scientific multi-lab 2000) has been examined to know about the composition of the elements and exact oxidation states of elements present in the GDS nanoparticles. The electrochemical experiments were performed using electrochemical workstations namely CV (CHI 1205C), and DPV (CHI 900) with a standard three-electrode configuration enclosing with SPCE, Ag/AgCl (saturated KCl), and platinum wire has been used as an operational electrode, reference electrode, and counter electrode. The complete electrochemical test was carried out in nitrogen gas (N_2) saturated conditions at laboratory temperature.

3. RESULTS AND DISCUSSION

3.1. PXRD and Raman study

To evaluate the crystalline nature and the phase structure of the as-prepared GDS, PXRD was executed and the corresponding results were pictured in Fig. 2A. The extensive diffraction peaks were noticed at $2\theta = 26.58, 29.53, 34.27, 37.96, 45.05, 49.26, 51.78, 58.51, 61.39, 72.23, 80.08, 82.45$, could be cataloged to (311), (222), (400), (331), (511), (440), (531), (622), (444), (800), (662), and (840), miller indices which are owned to the diffraction arrangements of cubic pyrochlore structure and also well matched with JCPDS No. 88-0456. At the same time, identical diffraction patterns also have been observed in the diffraction models of the fluorite defect. Commonly, the reflection planes of crystallographic planes of (111), (331), and (511) hkl planes belonged to the pyrochlore structure and entirely differentiated from the defective fluorite crystal structure. From Fig. 2A, two anemic peaks were obtained at $2\theta = 37.96^{\circ}, 45.05^{\circ}$ corresponding to the miller indices of (331) and (511) [51, 52]. The above conclusion proved that as-synthesized GDS nanoparticles exist as ($\text{Gd}_2\text{Sn}_2\text{O}_7$) cubic pyrochlore

structure without any other impurities. The as-prepared GDS pyrochlore owns the space group of $Fd-3m$ along with the determined lattice parameters $a = b = c = 10.45 \text{ \AA}$.

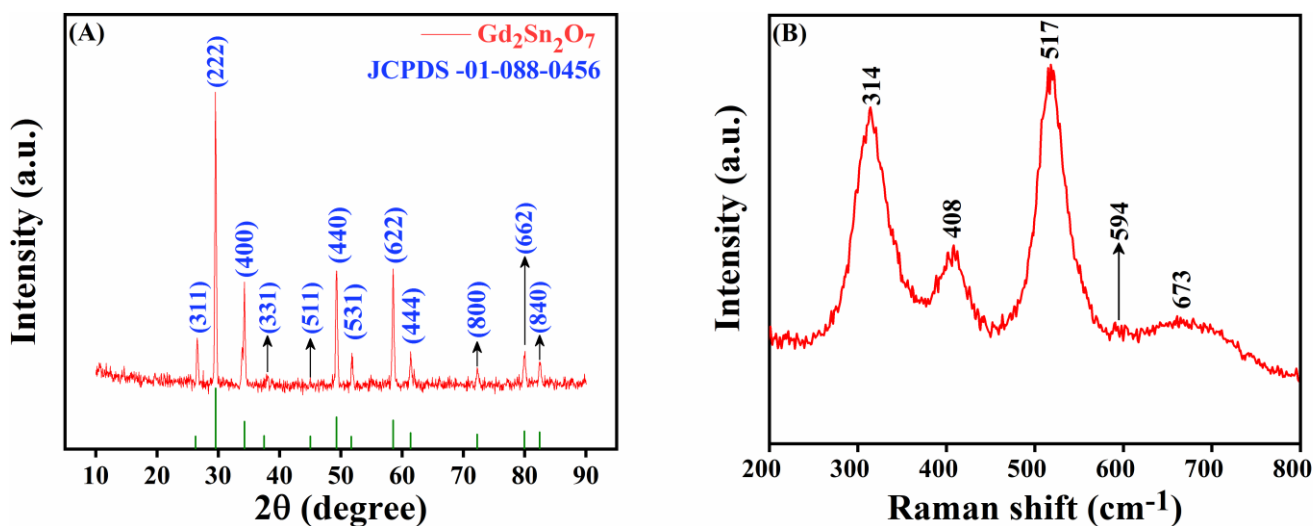


Figure 2. (A) PXRD patterns of GDS nanoparticles. (B) Raman spectroscopy of GDS nanoparticles.

Raman spectra is a very precise technique and it is used to investigate the disorder properties of the pyrochlore structure and also to analyze the metal-oxygen vibrational modes. The existence of vibrational modes of GDS was scrutinized with the help of Raman spectroscopy and pictured in Fig. 2B. According to the factor group analysis, the $A_2B_2O_7$ type of cubic pyrochlore structure shows six Raman modes such as $4F_{2g}$, A_{1g} , A_{1g} , and E_g , which belongs to the vibration of the $B-O_6$ Octahedron. Although F_{2g} modes correspond to the bending and stretching vibrations of A-O and B-O bonds. E_g mode speaks about the O-B-O bending vibrations. The figure shows three main broad peaks and two anemic peaks between $200-800 \text{ cm}^{-1}$. The vibrational band present at the 408 cm^{-1} belongs to the E_g mode, which can be attributed to the existence of O-Sn-O bending vibration. The Raman bands at 314 cm^{-1} , 594 cm^{-1} , and 673 cm^{-1} manifested the presence of F_{2g} mode lead to a mixture of stretching vibrations of Gd-O and bending vibrations of Sn-O. The high intense band at the 517 cm^{-1} corresponds to the A_{1g} mode due to the bending vibrations of Sn- O_6 . The above conclusion adequately matching with the already reported results [53, 54].

3.2. Surface characterizations

The textural observations of the as-prepared GDS nanoparticles were analyzed by FE-SEM and HR-TEM microscopic techniques with different magnifications. The observed FE-SEM histograms are outlined in Fig. 3A-C. In Fig. 3A-C, it is seen that the formation of irregularly shaped nanoparticles is evenly distributed in a regular arrangement.

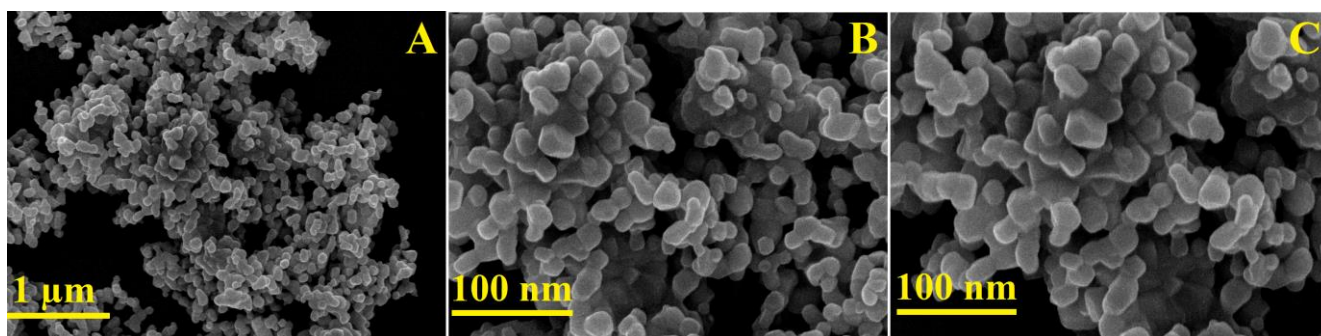


Figure 3. (A-C). FE-SEM images of the GDS nanoparticles with different magnifications.

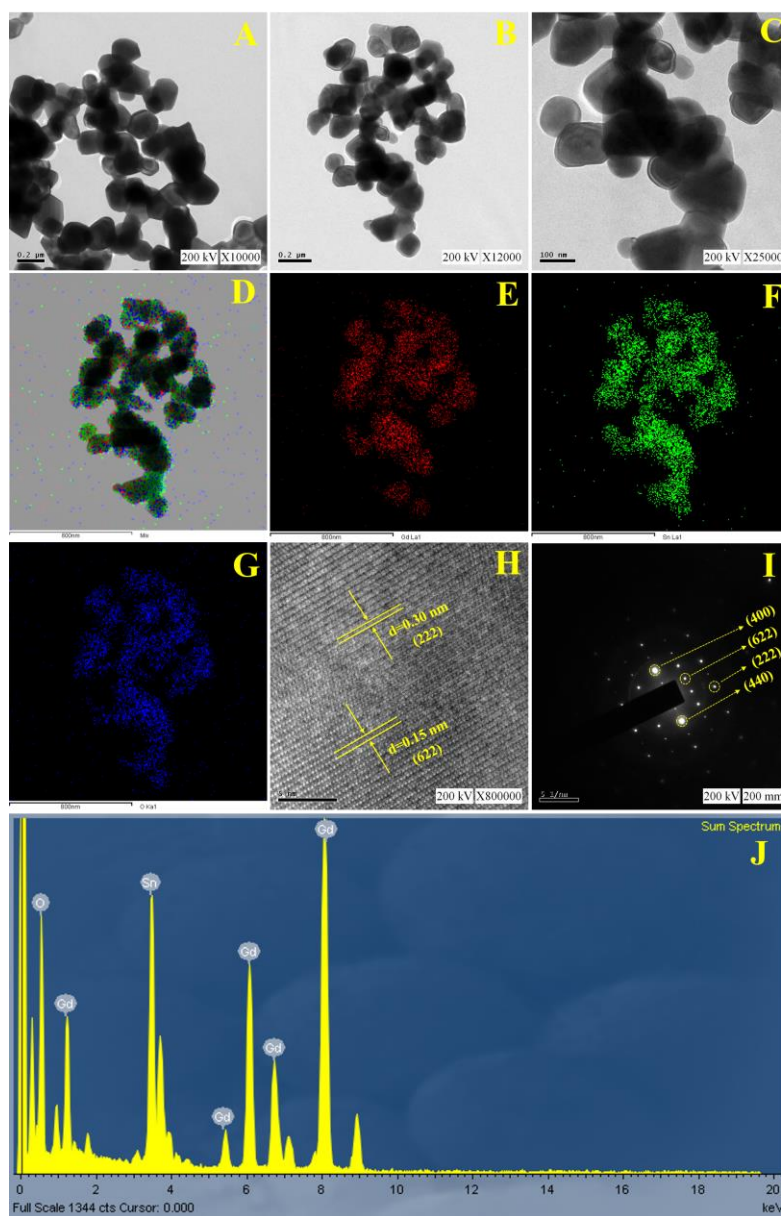


Figure 4. (A-C) shows the HR-TEM images in low and high magnification scales. (D-G) Elemental mapping observations of GDS nanoparticles. (H) Lattice fringes. (I) SAED ring patterns. (J) EDAX spectrum of GDS nanoparticles.

The average particle size of the as-prepared GDS was found to be 33 nm. In addition to that, the morphological observations of the GDS nanoparticles were investigated by using HR-TEM analysis. Interestingly, the acquired HR-TEM images exactly mimic the FE-SEM histograms and the obtained images are displayed in Fig. 4A-C. Fig. 4D-G shows the spatial distribution of the GDS nanoparticles with differently colored zonal compositions such as mixed mapping (red, blue, and green), red (Gd), green (Sn), and blue (O). All the elements (Gd, Sn, and O) are consistently scattered on the surface of $Gd_2Sn_2O_7$ without any other impurities and it is confirmed by elemental mapping analysis.

Fig. 4H displays the lattice fringes with an interatomic spacing of $d=0.15$ nm, and $d=0.30$ nm and it corresponded to the (622), (222) hkl plane values of the cubic pyrochlore $Gd_2Sn_2O_7$ nanoparticles. The selected area electron diffraction (SAED) patterns show the well-crystalline property of GDS cubic pyrochlore in Fig. 4I. The observed SAED brightest ring patterns are accorded well to the hkl plane values of (400), (622), (222), and (440) of the GDS nanoparticles and it is well-matched with the XRD findings. The EDAX spectrum from HR-TEM studies was shown in Fig. 4J, and it concludes the chemical composition of all the elements (Gd, Sn, and O) are presented in the GDS nanoparticles.

3.3. XPS analysis

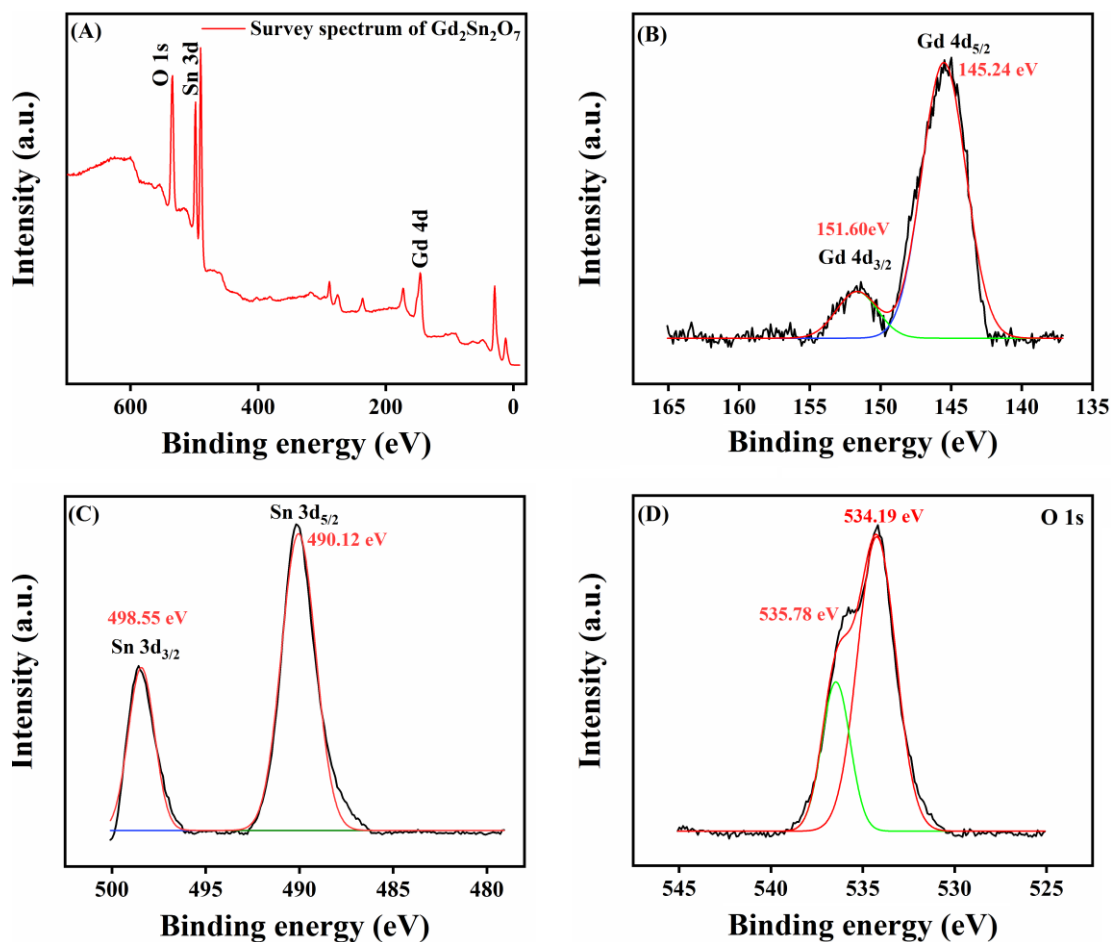


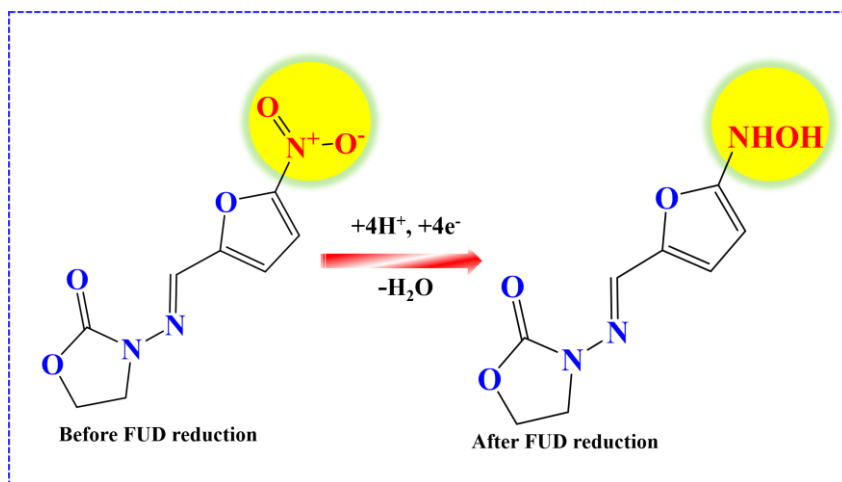
Figure 5. (A) XPS survey spectrum of GDS nanoparticles (B) Gd 4d, (C) Sn 3d, (D) O 1S

To attain precise data about the elemental findings and oxidation nature of the elements present in the GDS nanoparticles, X-ray Photoelectron Spectroscopy has been practiced and the obtained XPS spectra were portrayed in Fig 5.

The complete survey spectrum of GDS nanoparticles (Fig. 5A) established the existence of Gd, Sn, and O, which exactly matched with EDX results. To gain accurate electronic levels and their resembling binding energies, the survey spectrum was expanded in some particular ranges and the obtained high magnification results were depicted in Fig. 5 (B-D). Fig. 5B, shows the enlarged survey spectrum of Gd 4d which confirmed that the presence of Gd^{3+} as $4d_{5/2}$ and $4d_{3/2}$ ionic spin orbits were located at 145.2eV and 151.6 eV respectively [55]. The emphasized Sn 3d spectrum (Fig. 5C) displays the two well-defined peaks of Sn $3d_{3/2}$ and Sn $3d_{5/2}$ were noticed at 498.55 eV and 490.12 eV [56]. The elaborated survey spectrum of O 1S spectra (Fig. 5D) exhibits a meaningful peak at 534.19 eV and 535.7 eV, point out the presence of O^{2-} state [56]. It is verified from XPS results that the $Gd_2Sn_2O_7$ phase structure was consists of +3, +4, and -2 valance states of Gd, Sn, and O respectively.

3.4 Electrochemical reduction of Furazolidone (FUD) at GDS/SPCE

The electrochemical attitude of Furazolidone at GDS modified SPCE and unmodified SPCE was inspected by cyclic voltammograms (CV), and it is one of the predominantly existing analytical methods to estimating the electrochemical activity of electroactive substances. The CV was accomplished with 100 μ M of FUD over a wide potential range of 0.8 mV to -1.2 mV in N_2 saturated PBS (pH = 7.0) for GDS modified SPCE and bare SPCE at a steady sweep rate of 50 mV/s. From Fig. 6A, the bare SPCE (a) exhibits a current density of -13 μ A at a cathodic potential of -0.47 V, whereas the GDS modified SPCE shows a cathodic peak at -0.48 V along with higher current amplitude of -21.3 μ A. The GDS modified SPCE shows 1.61 fold higher current density compared to bare SPCE and the corresponding comparative bar diagram is depicted in Fig. 6B. However, there is no oxidizing peak obtained during the reverse scan in both modified and unmodified electrodes, which stands that the FUD reduction takes place at the surface of GDS modified SPCE should be an irreversible phenomenon. The irreversible reduction of FUD at the GDS modified SPCE electrode mainly resulted due to the conversion of (R- NO_2) nitro group of FUD to the corresponding hydroxylamine (R-NHOH) group which shows the transfer of the same number of electrons and protons ($4e^-$, $4H^+$) and also accompanied by the occurrence of FUD sensing followed by the reduction process [17]. Scheme 2 illustrates the corresponding FUD sensing mechanism at the GDS fabricated SPCE. The above mentioned earlier results established that GDS nanoparticles is a prenominal material and has good symbiotic behavior with superior electron-conducting active sites that facilitates the electron transfer property. In addition to that, it enables the effective sensing between the target analyte (FUD) and the electroactive material (GDS).



Scheme 2. The electrochemical sensing mechanism of FUD at GDS modified SPCE.

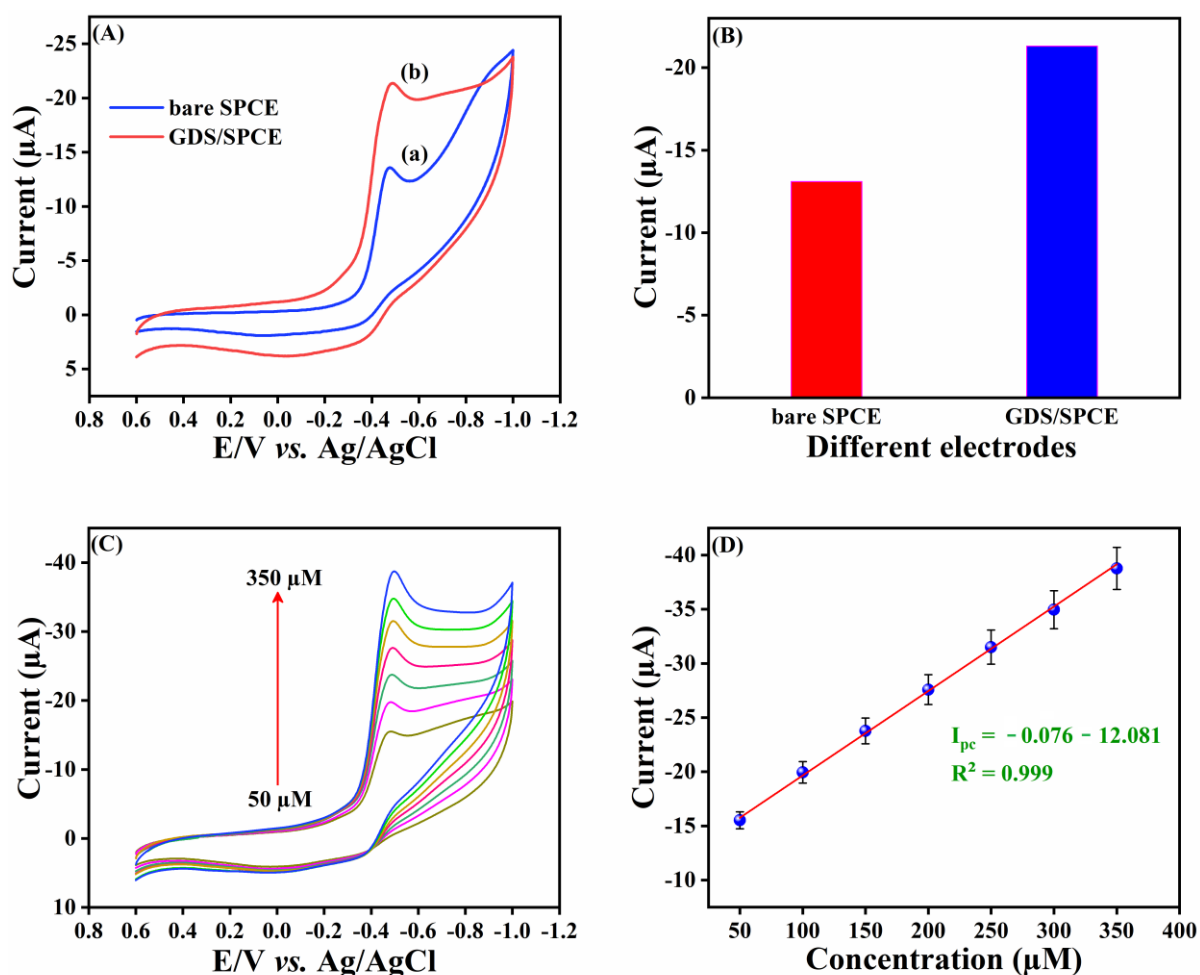


Figure 6. (A) Cyclic voltammograms results of bare SPCE (a), GDS modified SPCE (b) in the existence of 100 μM of FUD in 0.05 M PBS solution (pH 7.0) at a scan rate 50 mVs⁻¹. (B) Comparative bar diagram of different electrodes such as bare SPCE and GDS/SPCE. (C) CV response at GDS/SPCE with an increasing concentration of FUD from 50 to 350 μM. (D) A linear plot of concentration of FUD vs peak current.

In addition to that, the concentration effect of FUD at the surface of GDS fabricated SPCE was studied with differing the FUD concentration from 50 μM to 350 μM in pH 7.0. The effect of the addition test was performed at a sweeping amplitude of 50 mVs^{-1} and the corresponding results were illustrated in Fig. 6C. From Fig. 6C, it was witnessed that the cathodic current amplitude of FUD was heightened linearly while increasing FUD concentration from 50 μM to 350 μM . Fig. 6D outlines, the linear calibration curve with the correlation coefficient of $R^2 = 0.999$ along with a linear regression equation of $I_{\text{pc}} (\mu\text{A}) = 0.076 + 12.081$ was drawn for the obtained cathodic current amplitude vs FUD concentration.

3.5 Effect of pH and scan rate

Varying the pH of the electrolyte solution will cause symbolic effects on the electrochemical behavior of FUD. To inspect the effect of pH on the electrochemical reduction of FUD, CV was accomplished with the existence of 100 μM of FUD existing in 0.05 M PB solution of differing the pH values from 3.0 to 11.0, and the corresponding CV results were pictured in Fig. 7A. It can be shown that the reduction peak current of FUD was steadily raised with increasing the pH from pH 5.0 to 7.0. In the meantime, the peak current decreased when the pH value is above 7.0. This is because of the uncertainty of FUD in acidic and alkaline media. Fig. 7B, shows the comparison bar diagram of FUD reduction in various pH (5.0, 7.0, 9.0, and 11.0) which demonstrated that the maximal reduction peak current was observed in pH 7.0. So that, pH 7.0 was selected as a supporting electrolyte for the further electrochemical experiments.

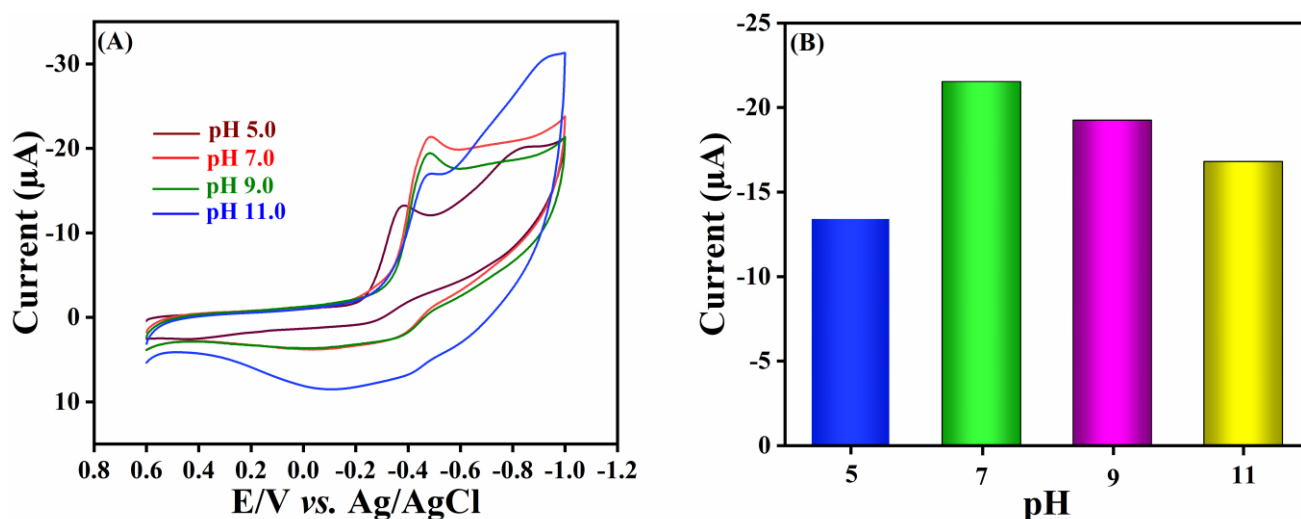


Figure 7. (A) CV performance of GDS/SPCE at a scan rate of 50 mVs^{-1} in different pH values such as 5.0, 7.0, 9.0, and 11.0. (B) Correlation bar diagram for different pH values vs cathodic current.

The scan rate studies give beneficial information about the kinetics of the reduction mechanism of FUD at the surface of GDS nanoparticles modified SPCE. To interrogate the influence of scan rate

on the reduction of FUD, CV was accomplished by differing the scan rate from 20 to 300 mV s⁻¹. The CV experiment was conducted in N₂ purged 0.05 M PB solution (pH 7.0) with the presence of 100 μM FUD. From Fig. 8A, it can be seen that the reduction peak current of FUD was linearly accelerated with expanding the sweeping rate from 20 to 300 mVs⁻¹. The respective linear plot between reduction peak current vs scan rate was pictured in Fig. 8B, along with a linear regression equation of $I_{pc} (\mu A) = -0.131 (mVs^{-1}) - 13.73$ and a correlation coefficient of $R^2 = 0.987$. Apart from that, the linear relationship was obtained between the square root of scan rate vs. peak current and the corresponded results were depicted in Fig. 8C along with a linear regression equation $I_{pc} (\mu A) = -3.013 (mVs^{-1})^{1/2} + 1.512$ and a correlation coefficient of $R^2 = 0.994$. The obtained results indicating that the electrode reaction process is driven by the diffusion process rather than the reaction controlled by the adsorption process. Using, Bard and Faulkner formula, the number of electrons involved in the electrochemical was derived from the attained CV results for the irreversible electrochemical reaction [57]. $E_p - E_{p/2} = 24$ mV which can be calculated from CV results and applied to equation (1)

$$E_p - E_{p/2} = (47.7/\alpha n) \text{ mV} \quad (1)$$

Deducing the equation (1), the value of αn was calculated to be 1.98. For a completely irreversible reaction, the value of electron transfer-coefficient (α) is considered to be 0.5. Upon substituting the α value in equation 1, gives the number of electrons was found to be 3.98, which is nearly equal to 4. Hence, the number of electrons for the cathodic reduction of FUD at the surface of GDS modified SPCE is known to be 4.

Relatively the peak potential move to a higher negative side in the potential window by increasing the amplitude of scan rate, which suggests the irrevocability of the reduction process. To understand the kinetics of FUD, heterogeneous electron transfer-coefficient K_s was calculated by Laviron's equation [58] by applying the slope value obtained from the calibration plot (Fig. 8D) drawn between E_{pc} vs. $\ln v$ (mVs⁻¹).

$$E_{pc} = E^0 + (RT/\alpha nF) \ln(RTK_s/\alpha nF) + (RT/\alpha nF) \ln v \quad \dots(2)$$

Where, v is the scan rate, n is the number of electrons (calculated to be 4.0), α is the electron transfer coefficient (assumed to be 0.5), T is the temperature (298 K), F is the Faraday constant (96485 C mol⁻¹), and E^0 is derived from the intercept of the E_{pc} vs. $\ln v$. From the Laviron's equation (2), heterogeneous electron-transfer coefficient K_s is calculated to be $8.6 \times 10^{-1} \text{ s}^{-1}$, which expose the electron transfer kinetics on GDS/SPCE for the reduction of FUD.

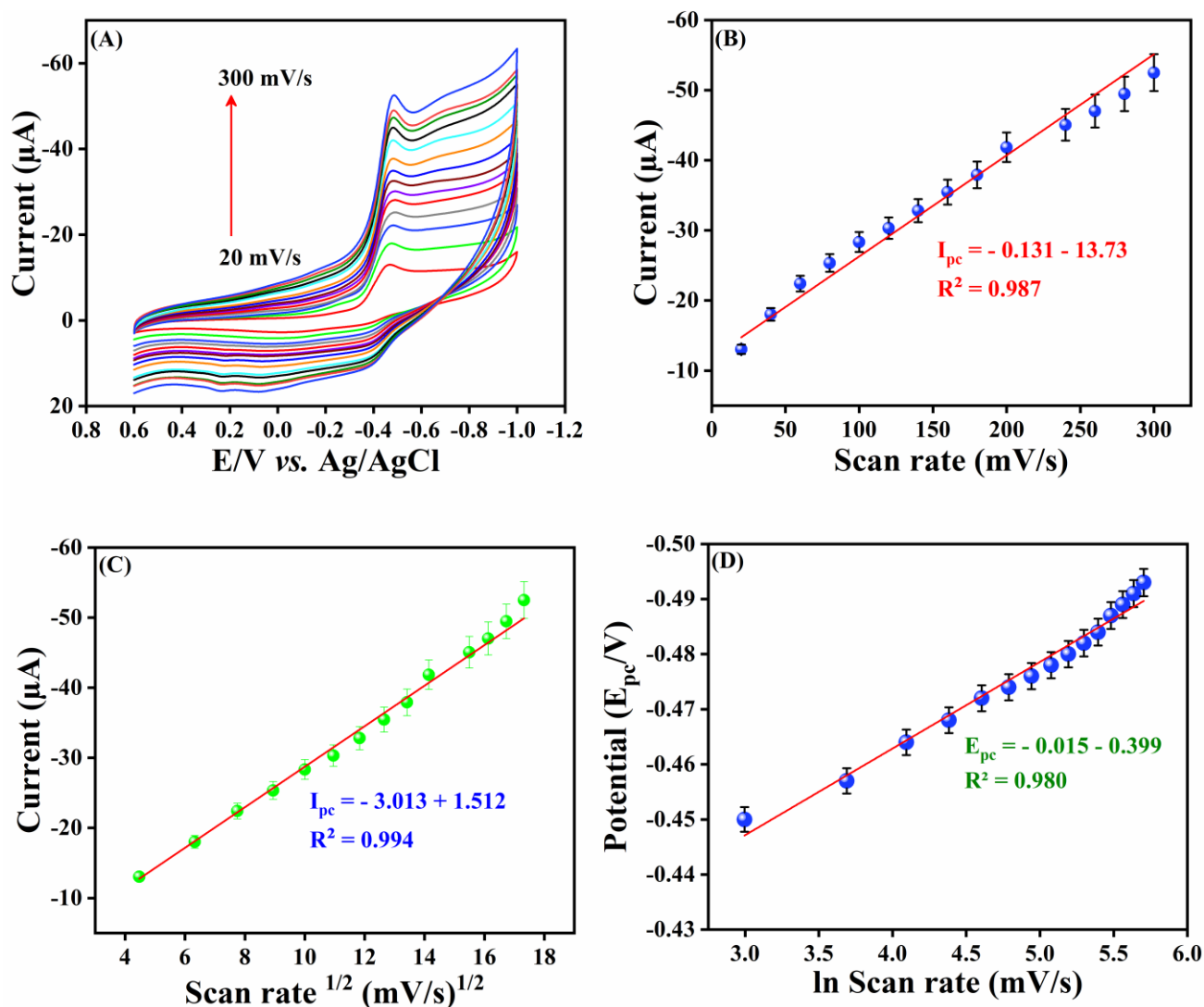


Figure 8. (A) The acquired CV signals for 100 μM FUD detection on GDS/SPCE in PB solution (pH = 7.0) at different scan rate interval from 20-300 mVs⁻¹. (B) The calibration plot between various scan rates vs. cathodic peak current. (C) The linear plot between the square root of scan rates vs. reduction peak current. (D) The linear plot between ln scan rate vs. peak potential.

3.6. Determination of Furazolidone

Differential pulse voltammetry (DPV) has a better resolution with a slight charging current involvement to the background current compared to CV. Hence, DPV was practiced to estimate the LOD, sensitivity of FUD at the surface of GDS nanoparticles modified SPCE. Fig. 9A exhibits the achieved reduction peak current of FUD at the GDS nanoparticles modified SPCE for various concentrations range starts with 0.01 μM to 1233 μM in PBS electrolyte (saturated with N₂) with the potential range between +0.6 to -1.2 V at a scan rate of 50 mVs⁻¹. From the obtained results, it has been shown that the reduction peak of FUD was increased when increasing the concentration FUD and expose the adequate linear relationship between the concentration of FUD and cathodic reduction signal. Fig. 9B, exhibits two wide linear plot which is achieved for the reducing peak current of FUD vs. the

concentration of FUD ranging from 0.01 to 153.21 μM and 193.21-1033.21 μM , their corresponding linear regression equations and its consistent correlation coefficients are $I_{pc} (\mu\text{A}) = -0.136 C_{\text{FUD}} (\mu\text{M}) - 10.383$; $R^2 = 0.959$ and $I_{pc} (\mu\text{A}) = -0.0346 C_{\text{FUD}} (\mu\text{M}) - 26.84$; $R^2 = 0.979$. Following the IUPAC convention, LOD was calculated to be 23 nm with the following formula;

$$\text{LOD} = 3\text{SD}/b \quad \dots(3)$$

In equation (3)

‘SD’ - the standard deviation of the background signal valuation

‘b’ - the sensitivity.

Furthermore, GDS/SPCE has a magisterial sensitivity of $0.66 \mu\text{A} \mu\text{M}^{-1} \text{cm}^{-2}$. The sensing execution of GDS/SPCE against FUD was compared with previously published results (Table 1). An efficient electrochemical result of FUD at GDS/SPCE occurs as the result of high surface area to improve as well to adsorb the desirable species GDS.

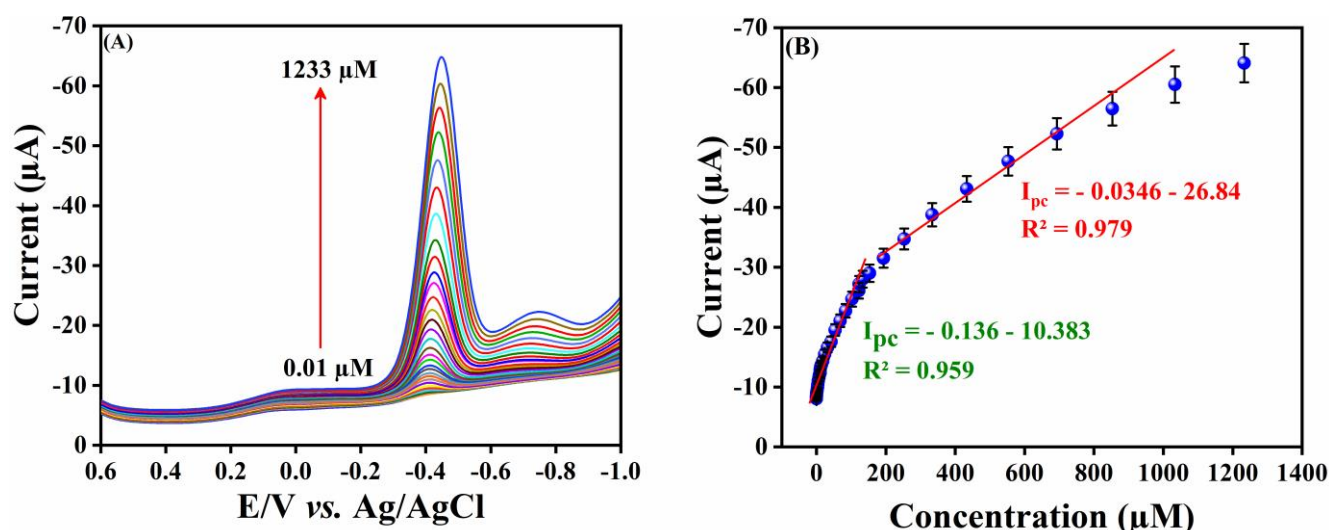


Figure 9. (A) The DPV performance of the GDS/SPCE for the successive addition of FUD concentration 0.01 μM to 1233 μM in PBS (pH = 7.0). (B) The linear plot for FUD concentration vs. cathodic reduction peak current.

3.7. Selectivity, repeatability, and stability studies

Selectivity is one of the important parameters for the newly designed sensor. To investigate the selectivity of GDS nanoparticles loaded SPCE for FUD, DPV was explored at a sweeping amplitude of 50 mVs^{-1} in PB solution (pH 7.0) under an N_2 atmosphere with the presence of some possibly interfering compounds. For this examination, some metal ions [Co^{2+} , Fe^{2+} , Mg^{2+} , and NO_3^-], biomolecules [ascorbic acid (AA), glucose (GLU), sucrose (SUC)], and similar nitro compounds [2-nitro phenol (2-NP), 4-nitrophenol (4-NP), nifedipine (NFDP), chloramphenicol (CLP)] were employed for evaluating the selectivity of the fabricated sensor. Accordingly, 20 times the excess concentration of biological molecules, metal ions, and 10-fold higher concentration of nitro compounds were introduced into the electrolytic cell containing 100 μM concentration FUD and the corresponding DPV response is

illustrated in Fig. 10A-C. The obtained DPV signals for metal ions (Fig. 10A), biological molecules (Fig. 10B), and nitro compounds (Fig. 10C) are displayed respectively. Interestingly, previously mentioned interfering compounds show insignificant peak current results associate with the FUD reduction peak current with a deviation of $\pm 7\%$. This exploration, obviously shown that the GDS/SPCE holds satisfactory selectivity achievement for FUD detection.

Table 1. The developed GDS modified SPCE was compared with previously reported FUD sensors.

Techniques	Electrode	linear range (μM)	LOD (nM)	Ref.
AMP ^a	Gr/Au/GCE	1-674	640	[17]
CV ^b	MWCNT/GCE	3-800	2300	[25]
DPV ^c	MWCNT/GCE	0.49-59	80	[59]
DPV ^c	GDS/SPCE	0.01-153.21	23	This work

^aAmperometry, ^bCyclic voltammetry, ^cDifferential pulse voltammetry, ^dLinear sweep voltammetry.

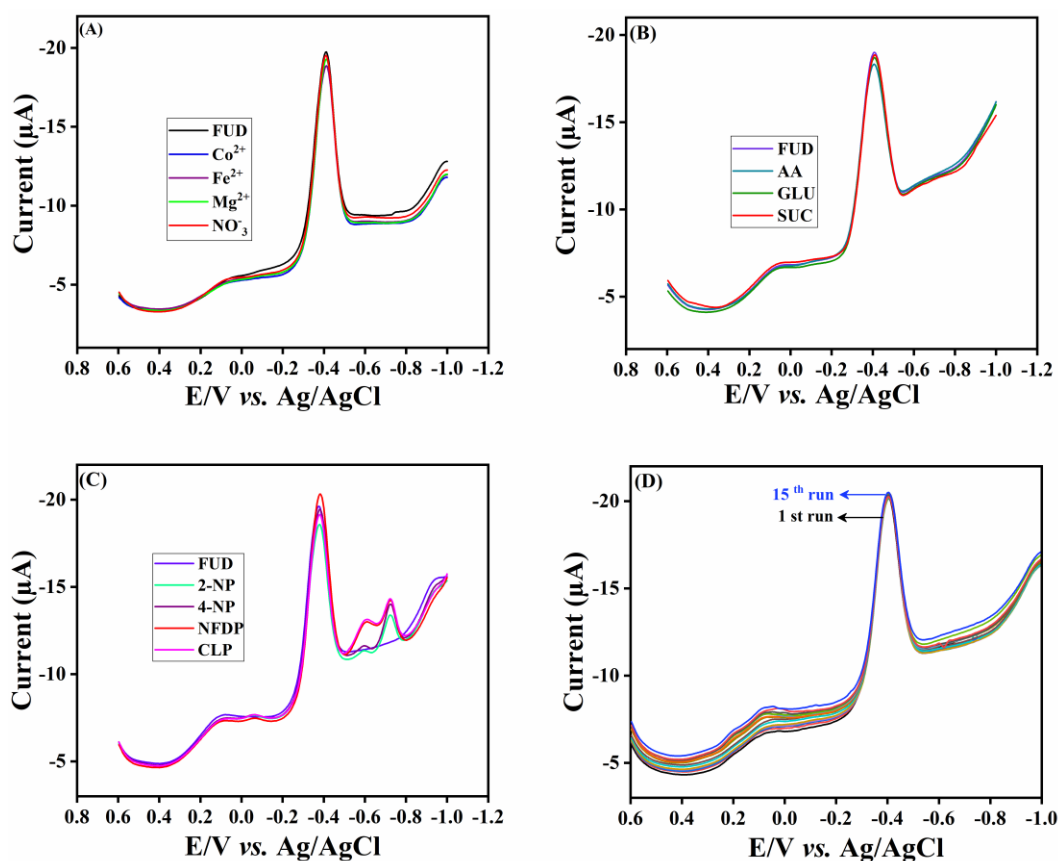


Figure 10. (A) DPV results of FUD reduction at GDS/SPCE in presence of ions (Co^{2+} , Fe^{2+} , Mg^{2+} , and NO_3^-). (B) DPV results of FUD reduction at GDS/SPCE in presence of biological molecules (AA, GLU, and SUC). (C) DPV results of FUD reduction at GDS/SPCE in presence of nitro compounds (4-NP, 2-NP, NFD, and CLP). (D) DPV results of repeatability test for FUD detection on GDS modified SPCE for 15 successive measurements.

The repeatability of the GDS fabricated SPCE was investigated by using the DPV technique, by the successive addition of 50 μM FUD in 0.05 M PBS (pH =7.0). For the repeatability evaluation of GDS/SPCE, 10 sequent measurements were executed with the single GDS/SPCE, and the acquired results are shown in Figure 10D and the RSD of the GDS/SPCE is 2.0% for the FUD sensing. Additionally, the storage capacity of the fabricated sensor was evaluated by the reduction peak current response of FUD over a time line up to 10 days. After 10 days, the constructed electrode holdup 96% of its elementary FUD peak current and the gathered results propose the valuable storage stability of the constructed GDS/SPCE. The above-obtained results exposed that the fabricated GDS/SPCE has exceptional accuracy, adequate repeatability, and admirable stability against FUD detection.

3.8 Real-time Analysis

To evaluate the realistic likelihood of the fabricated sensor for the real-time analysis, the GDS/SPCE was successfully tested to estimate the FUD concentration in tap water and lake water samples by utilizing the DPV technique. For the real-time analysis, the tap water was obtained from our laboratory and the lake water was collected from riverside Taipei. Before performing the experimental test, the collected water samples were filtered by Whatman filter paper to eliminate away some solid particles. Initially, the water samples are free from FUD and a known concentration of FUD is spiked and used up for the electrochemical studies. Utilizing the standard addition process, the FUZ addition samples and the obtained recovery value (94.5-99.5%) were calculated with the RSD value less than 3% and the corresponding results were outlined in Table 2.

Table 2. Electrocatalytic detection of FUD in water samples.

Sample	Added (μM)	Found (μM)	Recovery (%)
Tap water	5	4.9	98.0
	10	9.4	94.5
	15	14.5	97.0
	20	19.6	98.1
	25	24.2	97.0
Lake water	5	4.9	99.6
	10	9.5	95.0
	15	14.9	99.5
	20	19.4	97.5
	25	24.4	97.6

4. CONCLUSION

In this work, the GDS nanoparticles were effectively synthesized through a simple co-precipitation method. Crystalline purity and electronic states of the synthesized GDS nanoparticles have been examined by PXRD and XPS tools. In addition to that, the textural morphology of the as-prepared

GDS nanoparticles was observed by FE-SEM and HR-TEM analysis. Furthermore, the electroanalytical techniques namely the CV and DPV technique were employed for FUD detection. The constructed GDS/SPCE electrochemical sensor shows an admirable electrochemical activity for FUD sensing. Inspiringly, the above sensor exposed two linear ranges from 0.01-153.21 μM and 193.21-1033.21 μM and good sensitivity of 0.66 $\mu\text{A } \mu\text{M}^{-1} \text{ cm}^{-2}$. Besides, GDS nanoparticles were determined to have 23 nm of very low LOD. Meanwhile, the practicability of the constructed sensor was checked in water samples for real-time analysis. At the same time, GDS/SPCE sensor exhibited fine repeatability and storage stability. From the current work, all the achieved results have proved that the as-synthesized GDS nanoparticles had an efficient electrochemical activity towards FUD and it was applied as an encouraging electrode material for future application in pharmaceutical analysis.

References

1. T. Kokulnathan, S.M. Chen, *J. Hazard. Mater.*, 384 (2020) 121304.
2. B. Ji, J. Zhang, C. Zhang, N. Li, T. Zhao, F. Chen, L. Hu, S. Zhang, Z. Wang, *ACS Appl. Nano Mater.*, 1 (2018) 793–799.
3. V.N. Binh, N. Dang, N.T.K. Anh, L.X. Ky, P.K. Thai, *Chemosphere*, 197 (2018) 438–450.
4. L. Zhou, S.M. Limbu, M. Shen, W. Zhai, F. Qiao, A. He, Z.Y. Du, M. Zhang, *Environ. Pollut.*, 235 (2018) 245–254.
5. J.F. Kerrigan, K.D. Sandberg, D.R. Engstrom, T.M. LaPara, W.A. Arnold, *Sci. Total Environ.*, 621 (2018) 970–979.
6. P. Kowalski, A. Plenis, I. Olędzka, *Acta Pol. Pharm. - Drug Res.*, 65 (2008) 45–50.
7. E. Abo-Salem, J.C. Fowler, M. Attari, C.D. Cox, A. Perez-Verdia, R. Panikkath, K. Nugent, *Cardiovasc. Ther.*, 32 (2014) 19–25.
8. O.A. Alsager, M.N. Alnajrani, O. Alhazzaa, *Chem. Eng. J.*, 338 (2018) 548–556.
9. L. Oliferova, M. Statkus, G. Tsysin, O. Shpigun, Y. Zolotov, *Anal. Chim. Acta*, 538 (2005) 35–40.
10. A.L. Batt, D.D. Snow, D.S. Aga, *Chemosphere*, 64 (2006) 1963–1971.
11. M. Gros, M. Petrović, D. Barceló, *Talanta*, 70 (2006) 678–690.
12. M. Khodari, H. Mansour, G. A.m. Mersal, *J. Pharm. Biomed. Anal.*, 20 (1999) 579–586.
13. Z. Li, Z. Li, D. Xu, *Food Chem.*, 221 (2017) 1813–1821.
14. M. Annalakshmi, S. Sumithra, S.M. Chen, T.W. Chen, X.H. Zheng, *New J. Chem.*, 44 (2020) 10604–10612.
15. R. Fernando, D.M.S. Munasinghe, A.R.C. Gunasena, P. Abeynayake, *Food Control*, 72 (2017) 300–305.
16. M. Vass, K. Hruska, M. Franek, *Vet. Med. (Praha)*, 53 (2008) 469–500.
17. B.S. He, G.A. Du, *Anal. Methods*, 9 (2017) 4341–4348.
18. L. Fotouhi, S. Banafsheh, M.M. Heravi, *Bioelectrochemistry*, 77 (2009) 26–30.
19. J. Points, D. Thorburn Burns, M.J. Walker, *Food Control*, 50 (2015) 92–103.
20. A.A. Ensafi, M. Sohrabi, M. Jafari-Asl, B. Rezaei, *Appl. Surf. Sci.*, 356 (2015) 301–307.
21. R.J. McCracken, D.G. Kennedy, *J. Chromatogr. A*, 771 (1997) 349–354.
22. V. Arancibia, M. Valderrama, A. Madariaga, M.C. Zúñiga, R. Segura, *Talanta*, 61 (2003) 377–383.
23. K. Yin, W. Zhang, L. Chen, *Biosens. Bioelectron.*, 51 (2014) 90–96.
24. S. Ravisankar, M.J. Nanjan, M. Vasudevan, B. Duraiswamy, B. Suresh, N. Noorudeen, *Ind. J. Pharm. Sci.*, 60 (1998) 116–118.
25. L. Fotouhi, M. Nemat, M.M. Heravi, *J. Appl. Electrochem.*, 41 (2011) 137–142.

26. S. Shahrokhian, L. Naderi, M. Ghalkhani, *Mater. Sci. Eng. C*, 61 (2016) 842–850.
27. J.B. Raoof, R. Ojani, H. Karimi-Maleh, *J. Appl. Electrochem.*, 39 (2009) 1169–1175.
28. M. Fouladgar, H. Karimi-Maleh, *Ionics (Kiel)*, 19 (2013) 1163–1170.
29. H. Beitollahi, J.B. Raoof, H. Karimi-Maleh, R. Hosseinzadeh, *J. Solid State Electrochem.*, 16 (2012) 1701–1707.
30. H. Karimi-Maleh, M. Moazampour, H. Ahmar, H. Beitollahi, A.A. Ensafi, *Meas. J. Int. Meas. Confed.*, 51 (2014) 91–99.
31. H. Karimi-Maleh, M. Moazampour, A.A. Ensafi, S. Mallakpour, M. Hatami, *Environ. Sci. Pollut. Res.*, 21 (2014) 5879–5888.
32. A. Mohammadian, M. Ebrahimi, H. Karimi-Maleh, *J. Mol. Liq.*, 265 (2018) 727–732.
33. P. Balasubramanian, T.S.T. Balamurugan, S.M. Chen, T.W. Chen, G. Sharmila, M.C. Yu, *J. Taiwan Inst. Chem. Eng.*, 87 (2018) 83–90.
34. P. Balasubramanian, T.S.T. Balamurugan, S.M. Chen, T.W. Chen, T.W. Tseng, B.S. Lou, *Cellulose*, 25 (2018) 2381–2391.
35. J. Tian, H. Peng, X. Xu, W. Liu, Y. Ma, X. Wang, X. Yang, *Catal. Sci. Technol.*, 5 (2015) 2270–2281.
36. S. Gaur, D.J. Haynes, J.J. Spivey, *Appl. Catal. A Gen.*, 403 (2011) 142–151.
37. J. Lian, K.B. Helean, B.J. Kennedy, L.M. Wang, A. Navrotsky, R.C. Ewing, *J. Phys. Chem. B*, 110 (2006) 2343–2350.
38. B.J. Kennedy, B.A. Hunter, C.J. Howard, *J. Solid State Chem.*, 130 (1997) 58–65.
39. W. Wang, S. Liang, J. Bi, J.C. Yu, P.K. Wong, L. Wu, *Mater. Res. Bull.*, 56 (2014) 86–91.
40. H. Cheng, L. Wang, Z. Lu, *Nanotechnology*, 19 (2008).
41. H. Zhu, D. Jin, L. Zhu, H. Yang, K. Yao, Z. Xi, *J. Alloys Compd.*, 464 (2008) 508–513.
42. J. Zeng, H. Wang, Y.C. Zhang, M.K. Zhu, H. Yan, *J. Phys. Chem. C*, 111 (2007) 11879–11887.
43. M.A. Subramanian, G. Aravamudan, G. V. Subba Rao, *Prog. Solid State Chem.*, 15 (1983) 55–143.
44. N. Kim, C.P. Grey, *J. Solid State Chem.*, 175 (2003) 110–115.
45. B. J. Wuensch, K. W. Eberman, C. Heremans, E. M. Ku, P. Onnerud, E. M. E. Yeo, S. M. Haile, J. K. Stalick, J. D. Jorgensen., *Solid State Ion.* 129 (2000) 111–33.
46. C. Holt, M. Rahman, S.A. Akbar, P. Bulusu, C.C. Wang, *Mater. Lett.*, 40 (1999) 213–221.
47. J. Liao, L. Nie, Q. Wang, S. Liu, J. Fu, H.R. Wen, *J. Lumin.*, 183 (2017) 377–382.
48. S. Fujihara, K. Tokumo, *Chem. Mater.*, 17 (2005) 5587–5593.
49. J. Moon, M. Awano, K. Maeda, *J. Am. Ceram. Soc.*, 84 (2001) 2531–2536.
50. E. López-Navarrete, V.M. Orera, F.J. Lázaro, J.B. Carda, M. Ocaña, *J. Am. Ceram. Soc.*, 87 (2004) 2108–2113.
51. J.Y. Yang, Y.C. Su, Z. Chen, X.Y. Liu, *Adv. Mater. Res.*, 239–242 (2011) 2851–2854.
52. P. Duan, C. Han, Y. Zheng, G. Cai, F. Zhong, Y. Xiao, *J. Alloys Compd.*, 831 (2020) 154866.
53. K.M. Turner, C.L. Tracy, W.L. Mao, R.C. Ewing, *J. Phys. Condens. Matter*, 29 (2017).
54. L. Kong, I. Karatchevtseva, M.G. Blackford, N. Scales, G. Triani, *J. Am. Ceram. Soc.*, 96 (2013) 2994–3000.
55. C.V. Prasad, M.S.P. Reddy, V. Rajagopal Reddy, C. Park, *Appl. Surf. Sci.*, 427 (2018) 670–677.
56. Y. hai Gui, H. yan Wang, K. Tian, L. le Yang, H. shi Guo, H. zhong Zhang, S. ming Fang, Y. Wang, *Ceram. Int.*, 44 (2018) 4900–4907.
57. P.K. Brahman, L. Suresh, K.R. Reddy, J.S. Bondili, *RSC Adv.*, 7 (2017) 37898–37907.
58. S. Zhang, X. Zhuang, D. Chen, F. Luan, T. He, C. Tian, L. Chen, *Microchim. Acta*, 186 (2019).
59. L. S. Duan, L. Zhang, *J. Anal. Sci. Technol.*, 28 (2012) 673–676.

© 2021 The Authors. Published by ESG (www.electrochemsci.org). This article is an open access article distributed under the terms and conditions of the Creative Commons Attribution license (<http://creativecommons.org/licenses/by/4.0/>).